nature communications

Article

https://doi.org/10.1038/s41467-025-61909-5

A cytokine-based designer enzyme with an abiological multinuclear metal center exhibits intrinsic and extrinsic catalysis

Received: 18 October 2024

Accepted: 7 July 2025

Published online: 31 July 2025

Check for updates

Akiko Ueno[1,10], Fumiko Takida[1,10], Tomoki Kita[2], Takuro Ishii[1,3], Tomoki Himiyama[4] ✉, Takuya Mabuchi[5] ✉ & Yasunori Okamoto[1,6,7,8,9] ✉

A designer enzyme consisting of an abiological molecule incorporated into a natural protein has been developed as an exceptionally chemoselective catalyst, highlighting that the internal space of proteins is highly beneficial for enhancing catalytic performance. However, other features of proteins have received less attention in designer enzymes, for e.g., their use as ligands to construct abiological (multinuclear) metal centers and their intrinsic functions that have often been traded off for a new function. Here, grafting a synthetic trinuclear zinc complex inside a human cytokine macrophage migration inhibitory factor (MIF) scaffold using solely amino-acid side chains leads to a designer multi-metalloenzyme with extrinsic and intrinsic functions. The crystal structure of the designer tri-zinc enzyme verifies the accuracy of our design process based on geometry optimizations and quantum-chemical calculations. The extrinsic catalytic performance of this designer enzyme is of the highest class and comparable to that of previously reported designer zinc hydrolases. Importantly, an intrinsic function of MIF, i.e., its tautomerase activity, is maintained in this designer tri-zinc enzyme. Considering that cytokines are originally expressed in response to in vivo events, this cytokine-based designer metalloenzyme holds promising potential as a synthetic biological tool for the self-adaptive regulation of life phenomena.

In nature, a wide repertoire of chemical transformations are facilitated by enzymes. The use of metal ions in proteins further expands the reaction repertoire. For example, soluble methane monooxygenase, a diiron enzyme, facilitates methane hydroxylation, whilst nitrogenase, which possesses a cofactor consisting of eight iron atoms and a molybdenum atom, catalyzes nitrogen fixation. Furthermore, the oxygen-evolving complex (OEC) of photosystem II, which has a multinuclear metal cluster comprised of four manganese atoms and a calcium atom, oxidizes water to produce oxygen.

In such metalloenzymes, the protein scaffold plays two roles. Firstly, the amino-acid side chains act as ligands for fine control of the reactivity of the metal ions. Secondly, a well-defined internal space is created around the metal center to form a reaction compartment that enhances the reaction rate and chemoselectivity.

[1]Frontier Research Institute for Interdisciplinary Sciences, Tohoku University, Sendai, Miyagi, Japan. [2]Graduate School of Life Sciences, Tohoku University, Sendai, Miyagi, Japan. [3]Graduate School of Biomedical Engineering, Tohoku University, Sendai, Miyagi, Japan. [4]Molecular Biosystems Research Institute (MolBiS), National Institute of Advanced Industrial Science and Technology, Ikeda, Osaka, Japan. [5]Institute of Fluid Science, Tohoku University, Sendai, Miyagi, Japan. [6]The Exploratory Research Center on Life and Living Systems (ExCELLS), National Institutes of Natural Sciences, Okazaki, Aichi, Japan. [7]Research Center of Integrative Molecular Systems (CIMoS), Institute for Molecular Science (IMS), National Institutes of Natural Sciences (NINS), Okazaki, Aichi, Japan. [8]SOKENDAI (The Graduate University for Advanced Studies), Okazaki, Aichi, Japan. [9]PRESTO, Japan Science and Technology Agency, Kawaguchi, Japan. [10]These authors contributed equally: Akiko Ueno, Fumiko Takida. ✉e-mail: t-himiyama@aist.go.jp; mabuchi@tohoku.ac.jp; okamoto@ims.ac.jp

While synthetic model complexes have been developed with the aim of understanding such natural (multi)metalloenzymes[1,2], reproducing the well-defined enzymatic internal space responsible for high reactivity and selectivity remains challenging[3,4]. The significance of a protein as a reaction compartment has been elucidated in the studies on designer (metallo)enzymes that are constructed by incorporating catalytically active synthetic molecules, including metal complexes, into a protein. Thanks to the reaction compartment provided by the protein scaffold, enhanced reaction rates and high chemoselectivity have been achieved, while the incorporated synthetic molecule dictates the reaction type[5–12].

In contrast, the use of proteins as ligands currently lags behind their use as reaction compartments. This can be attributed to the difficulties associated with designing coordination-chemistry interactions between metal ions and amino-acid side chains at the atomic level. Hence, the development of designer mononuclear metalloenzymes has primarily relied on a more classical metal-substitution approach[13–16], meaning that the design of de novo metal-binding sites is even more challenging[17–22]. Although some excellent studies on the construction/mutualization of multinuclear metal centers using proteins and peptides as ligands have been reported[23–32], there are only a small number of examples of multinuclear metal centers that exhibit catalytic activity and the variety of the successfully used peptide/protein scaffolds is limited.

In addition to the exploitation of proteins as a ligand, the intrinsic functions of proteins have been afforded less consideration when constructing designer metalloenzymes. The primary consideration has usually been whether the protein possesses an internal space with appropriate size and shape, which is often responsible for its intrinsic function. Therefore, in hitherto reported designer metalloenzymes, the intrinsic function of the natural protein has often been traded off for a new function. On the other hand, nature has evolved proteins that possess multiple and independent functions, which are referred to as moonlighting proteins[33]. These moonlighting proteins exhibit different functions depending on their cellular localization, such as in the nucleus, cytoplasm, or extracellular space. The prevalence of these proteins among highly evolutionarily conserved enzymes suggests that they have evolved secondary functions over time. In other words, the acquisition of secondary functions by moonlighting proteins likely occurred not through a trade-off mechanism with primary functions, but rather through additive gains while maintaining their primary functions. The continuing utilization of the protein solely as a structural framework whilst overlooking the intrinsic function of the protein may reduce the rationale for the use of natural proteins in designer metalloenzymes, as compared to the rapidly emerging de novo proteins[34].

Nevertheless, prospective advantages of using natural proteins in designer metalloenzymes can be foreseen in their in celluo/vivo applications, especially where the designer enzyme orthogonally regulates life processes[35,36]. By enabling the installation of a new function into a protein while keeping its original function, similar to naturally evolved moonlighting proteins, designer metalloenzymes can be created that adaptatively exhibit an extrinsic functionality in relation to intrinsic biological processes, leading to promising tools for synthetic biology.

In this study, we aim to address two major challenges in the development of designer metalloenzymes: (i) the rational construction of a multinuclear metal center using a protein solely as a ligand, and (ii) preserving the intrinsic function of the scaffold protein.

Results and discussion

Building blocks and construction strategy for designer multimetalloenzymes

We focused on zinc as the metal center in this study because it is one of the most available metal ions in living systems[37]. Besides being a fulcrum point for the tertiary structure of the protein scaffold, the zinc ion functions as a catalytically active site in natural enzymes.

Mononuclear zinc active sites represent one of the most advanced developments in designer metalloenzymes[18,19,21,38–41]. Given that the construction of designer enzymes that bear mononuclear zinc sites in *E. coli* has been successfully demonstrated[17], designing non-natural multinuclear structures relying on zinc ions may be advantageous for future *in celluo/vivo* applications.

Some natural enzymes have a multinuclear zinc center, where the cooperative action of multiple zinc ions was found to be important for their catalytic activity[42]. However, compared to mononuclear zinc centers in designer enzymes, there are limited examples of functional multinuclear zinc centers, and in particular there are no examples with more than three centers.

Therefore, we aimed to graft a synthetic multinuclear zinc center into a protein scaffold, and thus we selected a catalytically active synthetic trinuclear zinc complex (Fig. 1a, b)[43]. In this complex three zinc ions are bridged by CO_3^{2-}, a structural motif that is not found in natural enzymes.

As a protein scaffold, we selected macrophage migration inhibitory factor (MIF), a cytokine involved in various physiological processes in vivo (Fig. 1c). We reasoned that the trimeric structure of MIF, specifically its internal pore, could be suitable for the transplantation of the trinuclear synthetic zinc complex. Moreover, the rigid secondary structure, comprised of β-sheets in the subunits that form the pore can be expected to facilitate the grafting of metal centers. Furthermore, MIF is an attractive scaffold to use here due to its multiple intrinsic functions as explained below[44–46].

MIF is encoded by the human *mif* gene and functions as an important regulator of innate immunity[44]. Upon stimulation with bacterial antigens or glucocorticoids, MIF is expressed and released from leukocytes. At the putative site shown in Fig. 1c, MIF binds to the CD74 receptor on other immune cells to activate a signaling pathway, which leads to gene transcription and the production of pro-inflammatory cytokines and chemokines for cell proliferation[47].

As shown in Fig. 1c, MIF is considered a moonlighting protein due to its multiple functions beyond its role as a cytokine. It exhibits phenylpyruvate tautomerase activity, whose physiological function remains enigmatic[45]. Furthermore, recent studies have revealed that MIF possesses nuclease activity. Upon association with the apoptosis-inducing factor, MIF degrades genomic DNA into large fragments within the nucleus, resulting in chromatinolysis. During this process, MIF is thought to primarily bind to 5′ unpaired bases in single-stranded DNA (ssDNA) with stem-loop structures[46]. The crucial sites for these functions are mainly located on the surface of MIF (Fig. 1c), suggesting that constructing a multinuclear zinc center within the pore is unlikely to compromise these intrinsic capabilities[45,47].

The binding sites for the zinc ions on the monomeric MIF were designed via the procedure outlined below. Each zinc ion of the synthetic trinuclear zinc complex is coordinated by three nitrogen atoms. Therefore, we selected a histidine residue as the sole ligand.

To analyze the optimal Cα atom positions for placing histidine residues in the pore of MIF, we conducted a systematic computational search. As shown in Fig. 2a, the z-axis was defined along the vertical axis of the pore. The three extracted zinc ions from the crystal structure of the synthetic complex were rotated in the x-y plane in 2° increments and translated along the z-axis in 0.5 Å increments whilst the distances, L_1, L_2, and L_3, between the Zn ions and the Cα atoms were cataloged. This comprehensive approach generated a total of 1281 different geometric configurations for evaluation. In this search, we confined the analysis to the upper region of the pore based on the preliminary hole-size analysis by MD simulations (Supplementary Fig. 1). Given that the entrance at the bottom of the pore is relatively larger than that at the top, we reasoned that the bottom entrance is more suitable for substrate uptake.

https://doi.org/10.1038/s41467-025-61909-5

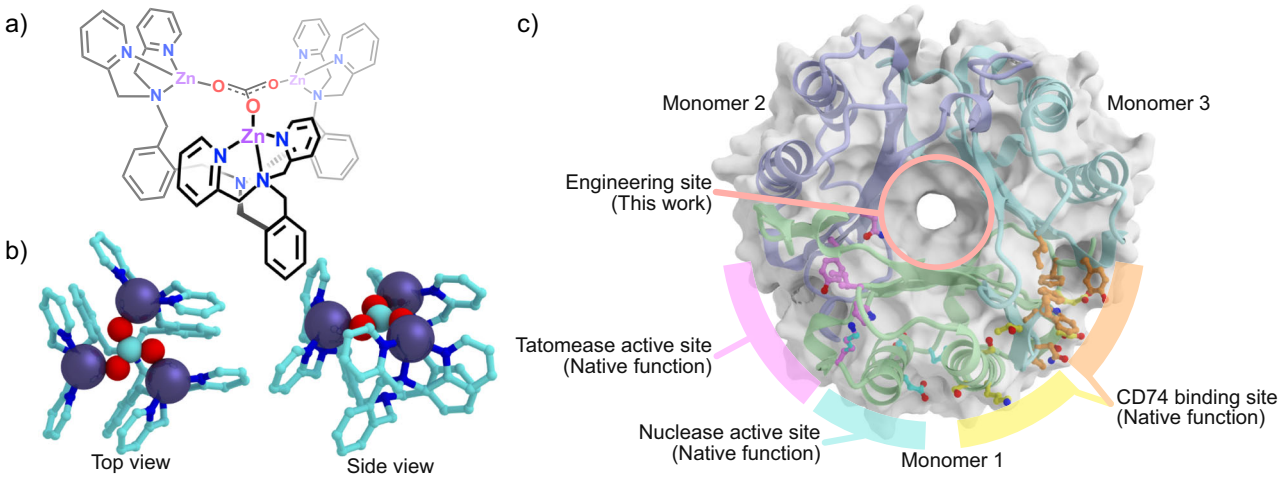

Fig. 1 | Building blocks used in this study to construct a designer tri-zinc enzyme. a Schematic and **b** crystal structures of the synthetic trinuclear zinc complex (CCDC 931956)[43], and **c** crystal structure of human MIF (PDB code: 1MIF), which is also known as a moonlighting protein, displaying the active sites for its multiple functionalities. The structural illustrations in this report were generated using CueMol2 (http://www.cuemol.org/en/). In (**b**), zinc, carbon, oxygen, and nitrogen atoms are shown in dark purple, cyan, red, and blue, respectively. **c** depicts oxygen in red and nitrogen in blue, while the carbon atoms are color-coded according to their functionality. Residues with carbon atoms in orange and yellow correspond to the CD74 binding site. Residues with the carbon atoms in cyan indicate the nuclease-active site, whereas those with carbon atoms in pink represent the tautomerase-active site.

The distances between the zinc ions and the Cα atoms of the coordinating histidine residues of natural zinc-binding proteins (PDB codes: 1AI0, 2CBA, 1IAG, 1TON, 1PQ4), which have three histidine residues as the sole ligands, often fall within the range of 6.0–6.7 Å. In case that one of the calculated distances (L_1, L_2, or L_3) fell outside of this range, the corresponding set of trinuclear zinc and Cα distances was excluded from the list. Thus, only triplets of Cα where all three Zn-Cα distances were within this biomimetic range were considered for selection. Candidate triplets for mutation were further filtered based on their geometric consistency, specifically requiring that the maximum difference among the pairwise distances ($|L_1-L_2|$, $|L_2-L_3|$, and $|L_1-L_3|$) was constrained to be <0.2 Å. Among the selected triplets, the following eight unique sets of Cα combinations appeared repeatedly: $S61_1$-$H63_1$-$Y100_1$, $S61_2$-$H63_1$-$Y100_1$, $S61_2$-$H63_1$-$Y100_2$, $S61_1$-$H63_1$-$N98_1$, $S61_2$-$H63_1$-$N98_2$, $H63_1$-$N98_1$-$Y100_1$, $H63_1$-$N98_2$-$Y100_1$, and $H63_1$-$N98_2$-$Y100_2$, where the subscript numbers denote the monomer on which these residues are located (Fig. 2a and Supplementary Table 1). Notably, His63 was consistently included in all of the selected triplets, despite not being explicitly required.

To further evaluate which combinations of Cα atoms are optimal for substitution with a histidine residue, we performed density-functional-theory (DFT) calculations for all eight triplets. According to the root mean square fluctuation (RMSF) analysis of wtMIF based on MD simulations prior to the DFT calculations, the residues selected through geometrical screening were found to be remarkably rigid (Supplementary Fig. 2). This observation suggests that consideration of backbone flexibility is not essential for subsequent DFT calculations aimed at identifying geometrically permissible Cα atom combinations to form a trinuclear site. Consequently, optimized models were calculated using three zinc ions, the CO_3^{2-} bridge, and nine histidine side chains without including the entire protein structure in order to keep computational expenses low. The coordinates of the main-chain atoms (N, Cα, and C) belonging to the β-sheet framework were extracted from the PDB (PDB code: 1MIF) and fixed, while the rest of the structure remained unconstrained. These model systems contained approximately 100 atoms in total.

As shown in Fig. 2b, energy differences obtained from the DFT-optimized structures suggested $S61_2$-$H63_1$-$Y100_2$, with two histidine residues introduced at the positions S61 and Y100 on the same monomer, and the original H63 on the other monomer, would yield the thermodynamically most stable trinuclear zinc center (Fig. 2b and Supplementary Table 2). The energy advantage of approximately 54.6 kcal/mol compared to the next most stable structure indicates this combination offers the optimal zinc-ion/histidine-residue interaction among the eight tested candidates.

Validation and optimization of the design via crystal-structure analysis

Henceforth, the designer zinc enzyme will be denoted as Zn_x-MIF, where x represents the number of zinc ions in the trimeric MIF. To validate our design strategy, we aimed to confirm the formation of the trinuclear zinc center via X-ray crystal-structure analysis.

The rationally designed MIF(S61H/Y100H) variant was expressed in *E. coli* BL21(DE3) and purified by ammonium-sulfate fractionation and anion-exchange column chromatography (Supplementary Figs. 3, 4, and Supplementary Table 3). The purified sample was crystallized using previously reported conditions[48], except for the addition of $ZnCl_2$. The X-ray crystal-structural analysis revealed that three zinc ions were bound in the pore of MIF (Supplementary Fig. 5a, d, g, and Supplementary Table 4). Furthermore, the presence of a bridging CO_3^{2-} ion was also confirmed, indicating that Zn_3-MIF(S61H/Y100H) had captured CO_3^{2-} ions dissolved in the solution under atmospheric conditions, given that CO_3^{2-} ions had not been used during the crystallization procedure. H61 of MIF(S61H/Y100H) is located slightly too far away from the zinc ion in order to coordinate with it when low-zinc-concentration conditions (10.5 eq per MIF monomer) were used for crystallization (Fig. 3c and Supplementary Fig. 5b, e, h). On the other hand, H63 and H100 coordinate with the zinc ion. While H61 and H63 maintain their original configurations with apo-MIF(S61H-Y100H), H100 flips to coordinate to the zinc ion.

Upon increasing the zinc concentration (26.0 eq to MIF), H61 flips to coordinate to the zinc ion (Fig. 3a–c and Supplementary Fig. 5b). These results indicate that H63 and Y100H are key residues for the coordination of zinc, and moreover, the presence of at least two histidine ligands would allow the formation of a trinuclear zinc complex. The three zinc ions, the CO_3^{2-} ion, as well as the H61, H63, and H100 residues in the crystal structure could be superimposed on the calculated structure with an RMSD of 0.709 Å, which validates our design strategy (Fig. 3g, h).

https://doi.org/10.1038/s41467-025-61909-5

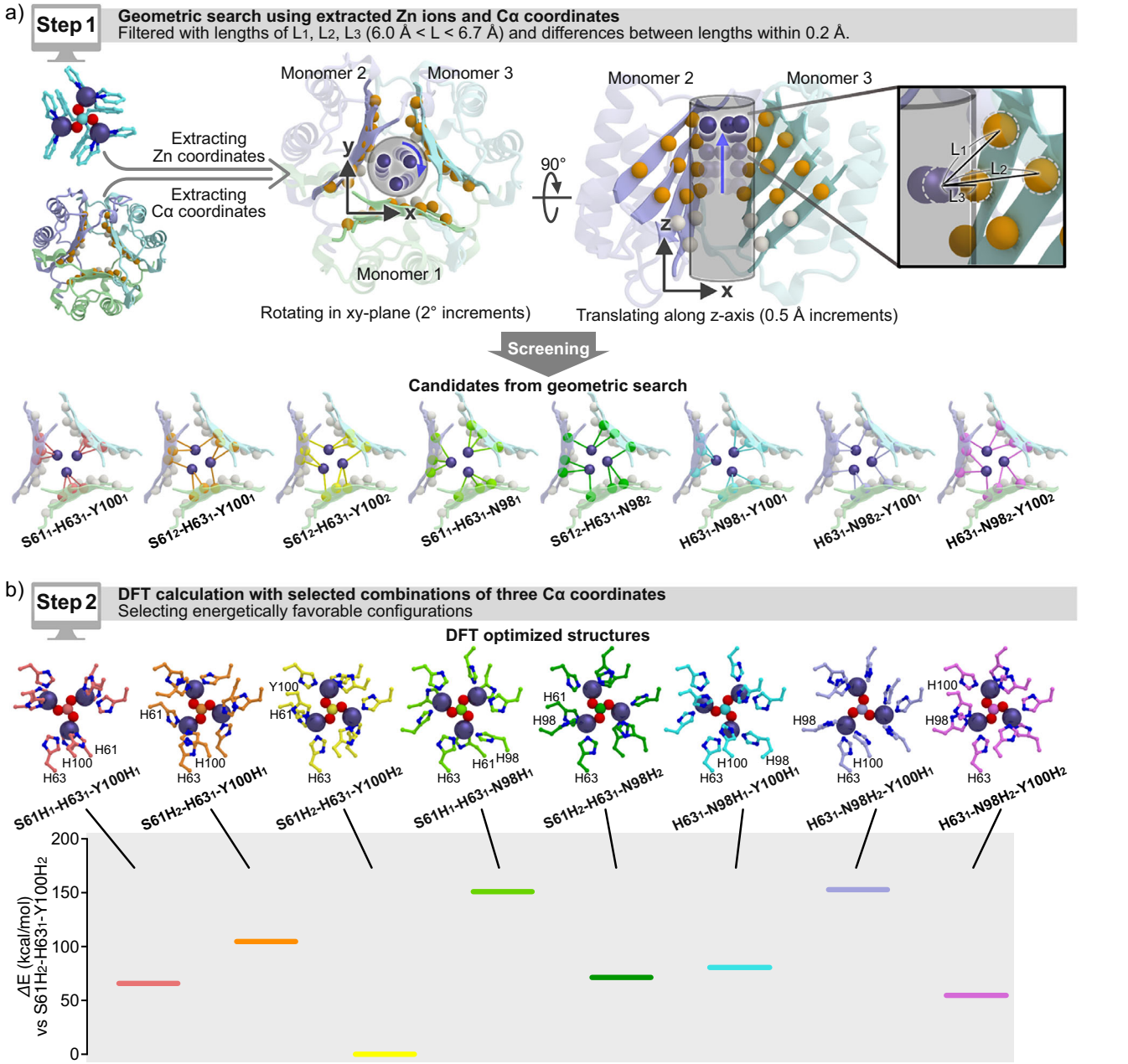

Fig. 2 | Workflow for designing a trinuclear zinc complex in MIF. a Schematic illustration of the computational search for the optimal positions of the Cα atoms to be substituted by histidine residues to coordinate the trinuclear zinc center. Spheres in deep purple represent Zn while those in orange or white represent Cα. The Cα sites in orange were selected for screening. Selected combinations of Cα and tri-zinc centers identified via a geometric search (Cα atoms and zinc shown as spheres). **b** Corresponding DFT-optimized structures with the selected histidine residues (zinc: purple; nitrogen: blue; oxygen: red). Structures represent $S61H_1$-$H63_1$-$Y100H_1$ (carbon: light red), $S61H_2$-$H63_1$-$Y100H_1$ (carbon: orange), $S61H_2$-$H63_1$-$Y100H_2$ (carbon: yellow), $S61H_1$-$H63_1$-$N98H_1$ (carbon: light green), $S61H_2$-$H63_1$-$N98H_2$ (carbon: green), $H63_1$-$N98H_1$-$Y100H_1$ (carbon: cyan), $H63_1$-$N98H_2$-$Y100H_1$ (carbon: blue), and $H63_1$-$N98H_2$-$Y100H_2$ (carbon: pink). The subscript numbers denote the monomer of MIF on which these residues are located. Estimated energy differences are displayed under the DFT-optimized structures. The colors of the bars in the energy diagram correspond to the carbon colors defined in the DFT-optimized structures described above.

Given the flexibility of the coordination modes of the zinc ion and the aforementioned observation that H61 is not necessarily essential, we prepared a variant with a single substitution, MIF(Y100H). Here, we assumed the presence of an abundant anion species such as OH^-, which can act as an active species for the hydrolysis reaction, and Cl^- to bind to the zinc center as an external ligand instead of the internal H61 ligand to compensate for the charge balance of the trinuclear zinc center.

Even when the low-zinc-concentration conditions were used, the corresponding crystal-structure analysis confirmed the presence of a trinuclear zinc center in Zn_3-MIF(Y100H) (Fig. 3d–f and Supplementary Fig. 5c, f, i). The configuration of H100 of Zn_3-MIF(Y100H) is identical to that of Zn_3-MIF(S61H/Y100H) under high-zinc-concentration conditions. As can be expected, the Cl^- ions bind to the zinc ion in Zn_3-MIF(Y100H). The trinuclear zinc center of Zn_3-MIF(Y100H) aligned well with the calculated structure with an RMSD of 0.900 Å (Fig. 3i).

Based on the fact that a trinuclear zinc center was confirmed to be present in MIF(Y100H), the H61 residue in Zn_3-MIF(S61H/Y100H) and the chloride ion in Zn_3-MIF(Y100H) could be labile ligands for the generation of a vacant site on the zinc ion during catalysis. Hence, we postulated that Zn_3-MIF(Y100H) could potentially be a better catalyst

https://doi.org/10.1038/s41467-025-61909-5

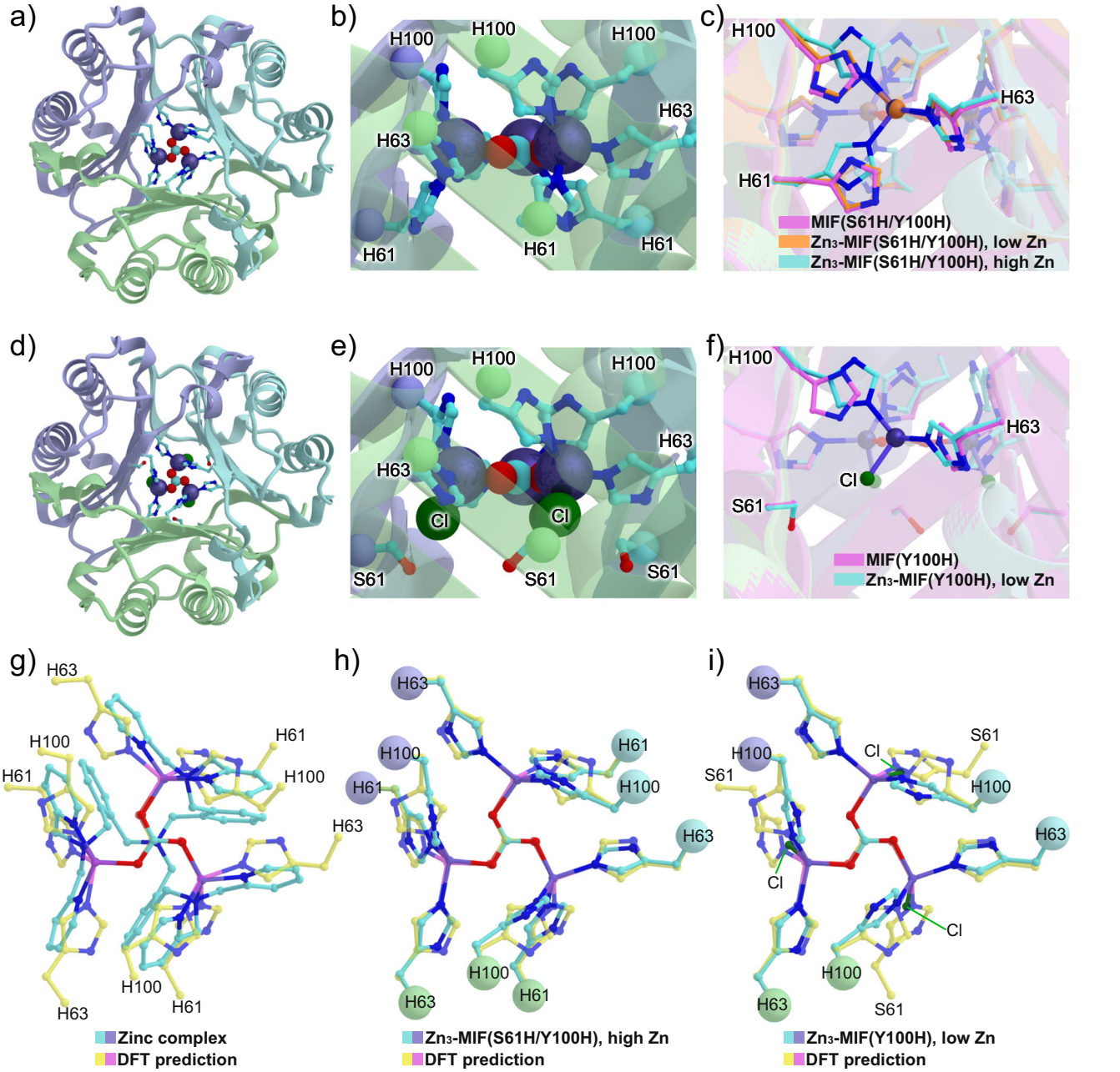

Fig. 3 | Crystal-structure analysis of the designer tri-zinc enzyme in this study. Top view of the crystal structures (**a**, **d**) and close-up side view (**b**, **e**) of Zn_3-MIF(S61H/Y100H) under high zinc concentration (PDB code: 9JIZ; carbon: cyan) and Zn_3-MIF(Y100H) (PDB code: 9JJ0; carbon: cyan). Superimposed images of the crystal structures: **c** MIF(S61H/Y100H) (PDB code: 9JIT; carbon: pink), Zn_3-MIF(S61H/Y100H) under low zinc concentration (PDB code: 9JIY; carbon: orange), and Zn_3-MIF(S61H/Y100H) under high zinc concentration; **f** MIF(Y100H) (PDB code: 9JIV; carbon: pink), and Zn_3-MIF(Y100H) under low zinc concentration. Superimposed images of the DFT-optimized trinuclear zinc center, $S61H_2$-$H63_1$-$Y100H_2$, (carbon: yellow) with **g** the synthetic zinc complex, **h** Zn_3-MIF(S61H/Y100H) under high zinc concentration, and **i** Zn_3-MIF(Y100H) under low zinc concentration (carbon: cyan). Carbon atoms are colored as described above. Zinc atoms are displayed in orange and deep purple for Zn_3-MIF(S61H/Y100H) under low zinc concentration and Zn_3-MIF(S61H/Y100H) under high zinc concentration, respectively. Other atoms are colored as follows: nitrogen (blue), oxygen (red), and chloride (green). Spheres represent Cα atoms, and the matching colors correspond to those of the same monomer.

than Zn_3-MIF(S61H/Y100H), which has a lower propensity to coordinate to zinc and a narrower space around the trinuclear zinc center where H61 likely hampers substrate access from the bottom (Fig. 3b, e).

Investigation of the Zinc-Binding Behavior of MIF(Y100H) in Solution

Next, we investigated the structure of Zn_3-MIF(Y100H) in solution. While the wild-type MIF (wtMIF) is thought to be a stable trimer in solution, dynamic-light-scattering (DLS) measurements were conducted to confirm whether MIF(Y100H) and Zn_3-MIF(Y100H) also exist as trimers (Fig. 4a and Supplementary Fig. 6). In the range of concentrations typically used for catalytic reactions of designer metalloenzymes, there was almost no difference between wtMIF and MIF(Y100H) in the presence or absence of zinc ions. The observed diameters are in good agreement with the crystal structures. These results suggest that MIF(Y100H) exists as a trimer and binds with a zinc ion in solution, as observed in the crystal structure.

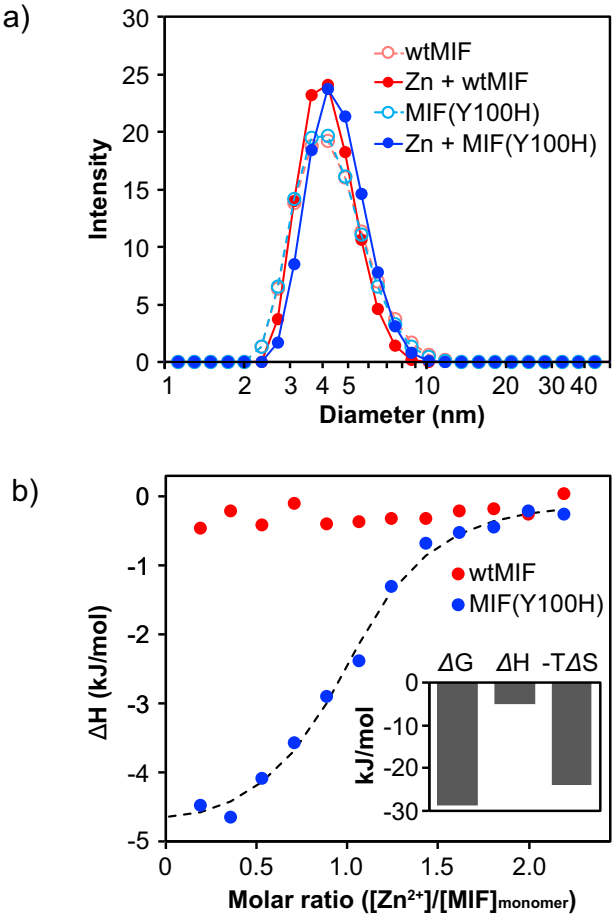

Fig. 4 | Solution structure of MIFs in the presence of zinc ions. a DLS measurements of wtMIF and the MIF(Y100H) variant. Experimental conditions: 100 µM MIF (monomer) and 100 µM $ZnCl_2$ in 10 mM MOPS buffer (pH = 7.9). **b** Binding isotherm of wtMIF and MIF(Y100H) as a function of the monomer protein to zinc ion concentration ratio. The fitting curve is displayed as a dashed black line. Experimental conditions: 150 µM MIF (monomer) was titrated with 1.7 mM $ZnCl_2$ in 10 mM MOPS buffer (pH = 7.9). Inset: thermodynamic parameters for the binding of Zn to MIF(Y100H).

To determine the stoichiometry and dissociation constant between the zinc ion and MIF(Y100H), isothermal titration calorimetry (ITC) was carried out (Fig. 4b). The corresponding results confirmed once more that three zinc ions bind with trimeric MIF(Y100H), which is consistent with the crystal structure of Zn_3-MIF(Y100H). The obtained titration curve fitted well to a typical 1:1 binding model, suggesting no cooperativity upon zinc-binding in trimeric MIF(Y100H). The dissociation constant between one zinc ion and monomeric MIF(Y100H) was determined to be 8.9 µM. In contrast to MIF(Y100H), no heat signal was observed in the case of wtMIF, suggesting that it lacks the ability to bind to zinc.

The thermodynamic parameters obtained for the binding of zinc to MIF(Y100H) suggest that the zinc binding was promoted by small enthalpy and large entropy changes (inset in Fig. 4b). This finding is in good agreement with those of a previously reported de novo copper enzyme[29].

Evaluation of the catalytic activity of the designer tri-zinc enzyme

To evaluate the catalytic activity of the trinuclear zinc center constructed in MIF(Y100H), we tested it in the hydrolysis of *p*-nitrophenyl acetate (pNA), which is a widely used benchmark reaction in designer zinc enzymes (Fig. 5a)[19,39].

No activity enhancement was observed when zinc ions were added in the presence of wtMIF, whereas the MIF(S61H/Y100H) mutant accelerated the reaction rate in the presence of zinc ions (Fig. 5b). Thus, the trinuclear zinc center formed in the MIF pore is deemed to be responsible for the acceleration of the hydrolysis. Next, the MIF(Y100H) variant was investigated. Even without the addition of zinc ions, some enhanced activity was observed for MIF(Y100H) compared to wtMIF. This might be attributed to the potential hydrolytic activity of the histidine residue itself, which has already been reported[49]. The most pronounced rate acceleration upon the addition of zinc ions was observed in the case of MIF(Y100H), thus verifying our rational design, which was intended to facilitate substrate access to the active site by removing His61 from MIF(S61H/Y100H) (Fig. 5b).

To investigate the time required for the formation of the zinc center, the initial rates of the hydrolysis reactions were measured by varying the incubation time after mixing the MIF and zinc ions. Over a range from 10 min to 24 h of incubation, no obvious differences were observed, suggesting that the zinc active center is formed quickly and is stable for several hours (Supplementary Fig. 9).

In general, a zinc-hydroxy species is the active intermediate that is formed during hydrolysis by a zinc enzyme. Assuming that the coordination of the chloride ion to the zinc ion observed in the crystal structure might compete with the coordination of H_2O and/or OH^-, the initial rate of hydrolysis in the presence of various NaCl concentrations was measured. As expected, the initial rate of hydrolysis by MIF(Y100H) in the presence of zinc ions decreased with increasing concentration of chloride ions (Supplementary Fig. 10). However, in the absence of zinc ions, this deceleration was not observed. Considering the possibility of a counter-cation effect, KCl was used instead of NaCl, resulting in a similar deceleration. These results indicate that the formation of the hydroxyl group on the zinc ion is in competition with the coordination of Cl^- to Zn.

The initial rates of hydrolysis catalyzed by MIF(S61H/Y100H) and MIF(Y100H) were measured in the presence of various equivalents of zinc ions (Fig. 5c). Consistent with the crystal-structure analysis discussed above, the bending points appeared at approximately 3 equivalents of zinc, indicating that both MIF(S61H/Y100H) and MIF(Y100H) bind with three zinc ions.

When trimeric MIF(Y100H) is used with three molar equivalents of zinc ions or less, the system produces four distinct species: MIF(Y100H); Zn_1-MIF(Y100H); Zn_2-MIF(Y100H); and Zn_3-MIF(Y100H). Considering the Zn-dissociation constant, almost all the zinc-binding sites of MIF(Y100H) are thought to be occupied in the presence of eight equivalents of zinc relative to trimeric MIF(Y100H). Under this concentration of zinc ions, Zn_3-MIF(Y100H) is the only species formed, and it is reasonable to conclude that this is when the initial rate reaches the plateau (Fig. 5c).

The initial rates of hydrolysis were measured again by changing the concentrations of the substrate. Using a comparison of the k_{cat}/K_M values, which is the slope of the linear fit of the activity plots in the low-substrate-concentration region, Zn_3-MIF(Y100H) exhibited approximately 1900% of the activity of its parent, wtMIF (Fig. 5d, e).

Several designer zinc enzymes have already been reported to exhibit high catalytic activity under basic conditions (pH = 9.5). Although Zn_3-MIF(Y100H) also shows a dependency on the pH in the range close to physiological conditions (pH = 6.7–7.9), it is not as pronounced as that observed for other designer zinc enzymes (Supplementary Fig. 11). The catalytic activity of Zn_3-MIF(Y100H) at pH = 7.9, $k_{cat}/K_M = 46.0 \pm 0.4\ M^{-1}s^{-1}$, represents a best-in-class value when compared with other designer zinc enzymes at their optimum pH (pH > 9.0)[18–21,38,39]. Zn_3-MIF (Y100H) retained 57% of its activity at pH = 7.9, even though the designer zinc enzymes reported in previous studies lose their activity at pH ≈ 7.0.

As mentioned in the ITC measurements, it was suggested that the binding of zinc to the three binding sites inside MIF is stochastic.

https://doi.org/10.1038/s41467-025-61909-5

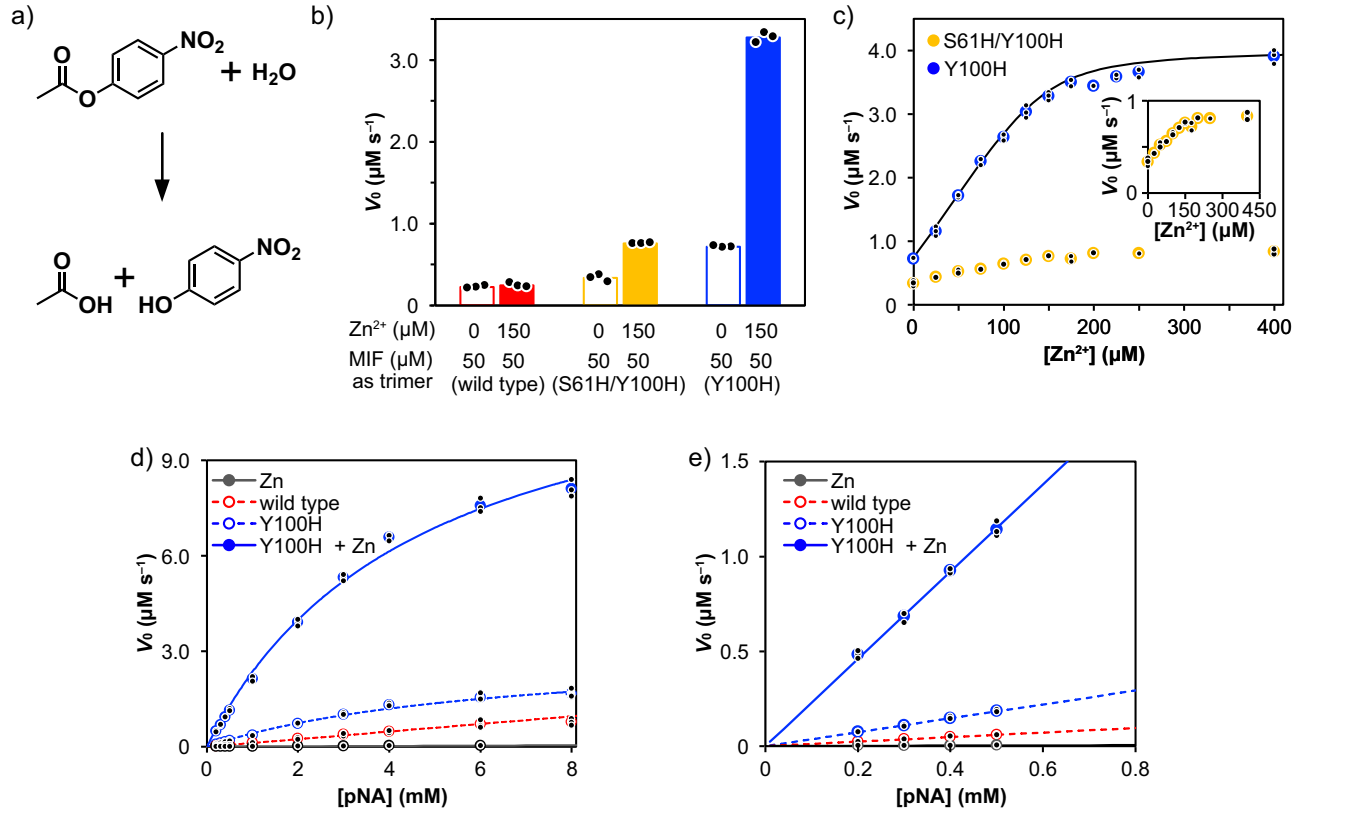

Fig. 5 | Extrinsic hydrolytic activity of the designer tri-zinc enzyme. **a** Benchmark hydrolysis reaction used in this study. **b** Comparison of the initial reaction rates of pNA hydrolysis catalyzed by wtMIF, the MIF(S61H/Y100H) variant, and the MIF(Y100H) variant in the absence and in the presence of $ZnCl_2$. Reaction conditions: 50 μM MIF (trimer), 150 μM $ZnCl_2$, 2 mM pNA in 50 mM MOPS buffer (pH = 7.9) at 25 °C. **c** Hydrolytic activity of the MIF(S61H/Y100H) variant (orange) and the MIF(Y100H) variant (blue) as a function of the concentration of Zn^{2+}. Reaction conditions: 50 μM MIF (trimer), 0–400 μM $ZnCl_2$, 2 mM pNA in 50 mM MOPS buffer (pH = 7.9) at 25 °C. The black solid line represents the theoretical regression (for details, see the section 'Estimation of the kinetic parameters' in the Supporting Information). **d**, **e** Michaelis–Menten plots of the hydrolytic activity of wtMIF and the MIF(Y100H) variant in the absence and presence of $ZnCl_2$. Reaction conditions: 50 μM MIF (trimer), 0 or 400 μM $ZnCl_2$, 0.2–8 mM pNA in 50 mM MOPS buffer (pH = 7.9) at 25 °C. The blue lines in (**d**) represent the regression curve of the Michaelis-Menten equation. The solid and dashed lines in (**e**) represent the linear regression curve based on the approximation of the Michaelis-Menten equation at low substrate concentrations. In this figure, colored bar-plots and dot-plots represent mean values from three independent experiments, whilst the corresponding individual data points are displayed as black dots.

Therefore, the ratios of four species at a fixed zinc-ion concentration can be mathematically estimated using the dissociation constant (Supplementary Fig. 12a). Individual k_{cat} and K_M values for both Zn_1-MIF(Y100H) and Zn_2-MIF(Y100H), which could not be isolated, can be estimated through regression analysis by using the initial rates of hydrolysis at different substrate concentrations in the presence of 0.5, 1.5, 3, and 8 equivalents of zinc, in combination with the calculated ratios of the four species (Supplementary Fig. 12b). This analysis suggests that Zn_2-MIF(Y100H) and Zn_3-MIF(Y100H) have smaller K_M values than Zn_1-MIF(Y100H) (Supplementary Fig. 12c, d), indicating that the second/third zinc atom might enhance the substrate binding as observed in natural multinuclear zinc enzymes. Thus, we have found evidence of the advantages that a multinuclear zinc site has compared to a mononuclear zinc site.

Evaluation of the intrinsic activity of MIF

Building on the success of imparting extrinsic function to MIF, we next investigated whether the intrinsic function of MIF is retained. As described above, MIF holds several independent functions related to life processes. As shown in Fig. 1c, most of the important amino-acid residues for these functions are placed on the surface of MIF. To confirm whether the newly installed tri-nuclear zinc center induces critical structural changes of these residues, which could potentially lead to complete impairing of their intrinsic functions, we focus here on one of the intrinsic functions, i.e., tautomerase activity, often assessed in structure-function-correlation studies, using isolated MIF and its variants (Fig. 6a)[50].

The initial rate of the tautomerase reaction was measured using 4-hydroxyphenylpyruvate (4-HPP) as the substrate (Fig. 6b). The reaction was catalyzed by wtMIF, and the addition of zinc ions did not affect the reaction rate. The initial reaction rate of MIF(Y100H) was slightly decreased compared to that using wtMIF.

While the residual activity of Zn_3-MIF(Y100H) decreased by 53% compared to that of wtMIF, the intrinsic function of the protein scaffold, which is typically lost in conventional designer metalloenzymes upon introduction of novel functionalities, was indeed preserved in the case of Zn_3-MIF(Y100H).

For the observed tautomerase-activity changes, the previous study indicated that the size of the pore formed at the trimer interface and the hydrogen-bond network between Y100 and H63 mediated by a water molecule within it have an allosteric effect on tautomerase activity, while the configurations of catalytic residues located on the surface involved in tautomerase activity hardly change between MIF variants with different levels of activity[45,48].

As shown in Fig. 6c, the positions and orientations of catalytic tautomerase residues in wtMIF, MIF(Y100H), and Zn_3-MIF(Y100H) structures are nearly identical. On the other hand, however, a comparison of the crystal structures revealed that the water-mediating

https://doi.org/10.1038/s41467-025-61909-5

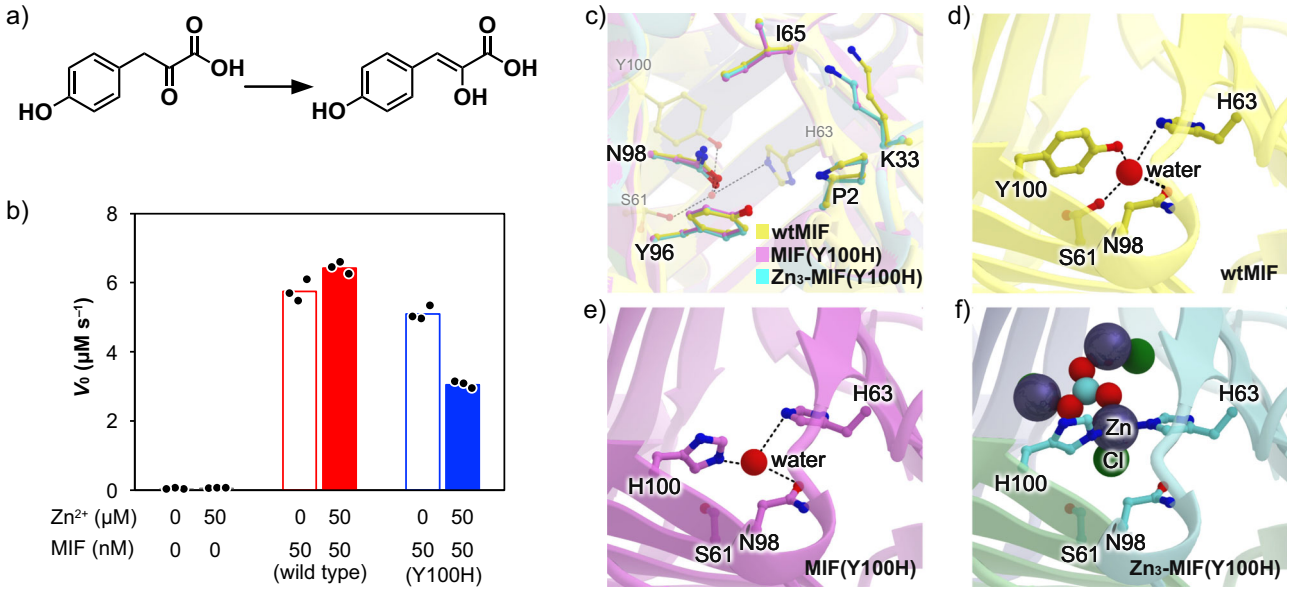

Fig. 6 | Intrinsic tautomerase activity of the designer tri-zinc enzyme Zn_3-MIF(Y100H). a The benchmark tautomerization reaction used in this study. **b** Comparison of the reaction rates of tautomerization catalyzed by wtMIF and the MIF(Y100H) variant in the absence and presence of $ZnCl_2$. Reaction conditions: 50 nM MIF (trimer), 50 μM $ZnCl_2$, 2 mM 4-HPP in 1 M borate buffer (pH = 6.2) at 25 °C. The colored bar-plots and black dot-plots represent mean values and individual data from three independent experiments, respectively. **c** Superimposed crystal structures around the active sites for tautomerase activity in wtMIF (PDB code: 3DJH), MIF(Y100H), and Zn_3-MIF(Y100H). Comparison of water-molecule networks in (**d**) wtMIF, (**e**) MIF(Y100H), and (**f**) Zn_3-MIF(Y100H), which are presumed to be important for tautomerase activity[48]. Carbon atoms are colored by variant (yellow: wtMIF; pink: MIF(Y100H); cyan: Zn_3-MIF(Y100H)); other atoms: zinc (deep purple), nitrogen (blue), oxygen (red), and chloride (green).

hydrogen-bonding network between H63 and Y100 present in wtMIF was preserved in MIF(Y100H) but disrupted in Zn_3-MIF(Y100H) upon zinc-ion binding (Fig. 6d–f). These observations align well with findings from the previous research[48].

Given that the biological role of tautomerase activity is still not fully understood, it is not clear whether the observed decrease in tautomerase activity is a critical dysfunction to maintain vital functions. However, the tautomerase activity observed in this study remains within the same order of magnitude as that of wtMIF. Thus, as designed, both the intrinsic and extrinsic functions have been successfully retained and implemented.

In summary, we have succeeded in reproducing the structure of a synthetic trinuclear zinc complex in the internal space of the trimeric macrophage migration inhibitory factor (MIF) protein based on intuitive computational design. Our computational pipeline, which does not require drastic quantities of computational resources, significantly reduces experimental efforts, given that we were able to focus on the most promising variant and prepare only two variants, i.e., the identified lead candidate and one additional derivative. Additionally, our simple pipeline can be easily adapted for the grafting of other multinuclear synthetic complexes.

The designer tri-zinc enzyme, Zn_3-MIF(Y100H), shows a top-tier activity compared to previously reported designer mononuclear zinc hydrolases, one of the most well-developed designer metalloenzymes. In contrast to the conventional approaches of reproducing and miniaturizing metalloenzymes, this study aimed at demonstrating that proteins can be used like small synthetic molecular ligands by synthesizing an unnatural multinuclear metal center using solely amino-acid side chains.

In addition, our designer tri-zinc enzyme exhibits not only the extrinsic function derived from the trinuclear zinc center but also retains the intrinsic functions of the wild-type MIF, something that is often sacrificed in favor of the extrinsic function in other designer enzymes. Given that MIF is produced, secreted, and translocated between cells by sensing cellular environments, harnessing its inherent disposition could allow developing designer enzymes that are autonomously produced within the body in response to physiological conditions and synthesize pharmaceuticals and/or induce any perturbation to change the physiological condition. The key discovery in this study is that grafting a trinuclear zinc center has minimal impact on the surface-derived functionality. This finding is crucial as it enables us to proceed to the next stage of our research, i.e., the integration and utilization of this designer multi-metalloenzyme in concert with cellular functions, leading to a synthetic-biology tool for the self-adaptive regulation of life phenomena[51]. Consequently, this report demonstrates some advantages of using natural proteins as scaffolds for designer metalloenzymes, even in light of the rapidly growing field of de novo proteins.

While the tandem reaction between hydrolysis and tautomerase activity is interesting and newly installed hydrolysis activity can be potentially exploited for the deprotection of caged drugs, it is desirable that the reaction promoted by the designer enzyme is biorthogonal. Thus, we are currently exploring non-natural reactivity by constructing other multinuclear centers based on the approach presented in this study.

Methods

Mutation candidate identification

We used a Python script to narrow down mutation candidates based on distance analysis. From the wild-type structure (PDB code 1MIF), we extracted the coordinates of the Cα atoms of the amino-acid residues on the inner β-sheet, which we refer to as the MIF-Cαcoordinates. Additionally, we extracted the Zn coordinates from the crystal structure of the Zn tri-nuclear synthetic complex (CCDC 931956), referred to as the Tri-Zn coordinates. The MIF-Cα coordinates were rotated around the symmetry axis of the pore along the z-axis such that the center of mass was positioned at $z = 0$ and the N-terminal end was oriented toward the +z direction. The Tri-Zn coordinates were aligned parallel to the xy-plane and translated along the z-axis in 0.5 Å

increments within the range of 0–10 Å. At each z-coordinate, the Tri-Zn coordinates were rotated in 2° increments within the range of 0–120°, resulting in a total of 1281 points where the distance between the Cα and Zn was calculated. For each Zn atom, the three closest Cα atoms were identified within a distance range of 6.0–7.0 Å. Among all possible triplets, those in which the difference between the maximum and minimum of the three Cα–Zn distances was <0.2 Å were selected as candidates to ensure geometric uniformity. Triplets containing duplicated residue numbers were excluded. Based on this screening, a total of eight representative coordination candidates, i.e., $S61_1$-$H63_1$-$Y100_1$, $S61_2$-$H63_1$-$Y100_1$, $S61_2$-$H63_1$-$Y100_2$, $S61_1$-$H63_1$-$N98_1$, $S61_2$-$H63_1$-$N98_2$, $H63_1$-$N98_1$-$Y100_1$, $H63_1$-$N98_2$-$Y100_1$, and $H63_1$-$N98_2$-$Y100_2$, were selected for further DFT calculations.

DFT calculation

Based on the results from the Python analysis, we performed structural optimizations using density-functional-theory (DFT) calculations for eight selected candidates, i.e., $S61_1$-$H63_1$-$Y100_1$, $S61_2$-$H63_1$-$Y100_1$, $S61_2$-$H63_1$-$Y100_2$, $S61_1$-$H63_1$-$N98_1$, $S61_2$-$H63_1$-$N98_2$, $H63_1$-$N98_1$-$Y100_1$, $H63_1$-$N98_2$-$Y100_1$, and $H63_1$-$N98_2$-$Y100_2$. The DFT calculations included three zinc ions, the CO_3^{2-} bridging group, and nine histidine side chains with hydrogen atoms added, but excluded the larger protein structure. The coordinates of the main-chain atoms (N, Cα, and C) belonging to the β-sheet framework were fixed to preserve the protein backbone structure, while the remaining atoms were fully relaxed. All of the geometry optimizations were performed at the PBE1PBE-GD3BJ/6–31 G(d,p) level in the Gaussian 16 package (version ES64L-G16RevC.01)[52].

Molecular dynamics simulations

All-atom molecular dynamics (MD) simulations were performed with the CHARMM36m force field[53] using the LAMMPS software[54]. Atomic coordinates of human MIF were taken from the Protein Data Bank (PDB code: 1MIF). The MIF structure was placed in a periodic simulation box and solvated by adding water. The salt concentration was set to 0.15 M NaCl, and the corresponding numbers of Na^+ and Cl^- ions were added. After the steepest-descent energy minimization, the systems were equilibrated for 1 ns in the NPT ensemble at 300 K and 1 atm. Production runs were then performed for 100 ns in the NPT ensemble at 300 K and 1 atm, and the trajectory data were collected every 10 ps. The temperature was maintained with a Nosé–Hoover thermostat[55,56] and the pressure was controlled with a Parrinello–Rahman barostat[57,58]. The nonbonded interactions were calculated with a cutoff distance of 1.2 nm, and the particle–particle particle–mesh (PPPM) method[59] was used to calculate long-range electrostatic interactions. The equations of motion were integrated using the Verlet algorithm[60] with a time step of 2 fs, along with the SHAKE algorithm[61] to constrain the lengths of bonds to hydrogen. The root mean square fluctuations (RMSFs) of Cα atoms for each residue were calculated with respect to the average structure obtained from the last 30 ns of the trajectories. The time-averaged pore radius and its standard deviations along the Z-coordinate were also computed over the last 30 ns using the HOLE program[62]. VMD[63] was used to generate the images.

Protein expression, purification, and crystallization

As listed in Supplementary Table 3, expression plasmids for the wild-type MIF, the S61H/Y100H variant, and the Y100H variant were transformed into *E. coli* BL21(DE3). A single colony of the transformed cells was inoculated into 10 mL of Luria-Bertani broth (LB) containing 50 μg/mL of ampicillin and 1% (w/v) glucose and incubated at 37 °C until the OD_{600} reached 0.8. The resulting culture was then inoculated into 700 mL of LB medium containing 50 μg/mL of ampicillin to give a final OD_{600} of 0.002 and incubated aerobically with vigorous shaking at 37 °C. When the OD_{600} reached between 0.8 and 1.0, the culture was cooled on ice for 10 min. Isopropyl β-D-1-thiogalactopyranoside (IPTG) was added to a final concentration of 0.4 mM to induce protein expression. The resulting culture was then incubated at 20 °C overnight with shaking, and the cells were harvested by centrifugation (4000 × g at 4 °C for 15 min) and stored at −80 °C.

The frozen harvested cells from the 700 mL culture were resuspended in 30 mL of 20 mM Tris-HCl buffer (pH = 7.4, adjusted at 4 °C) and lysed by sonication. $MgCl_2$ was added to the lysate to give a final concentration of 1 mM, followed by the addition of DNase I (20 units). After a 20 min incubation on ice, streptomycin sulfate was added to the mixture to give a final concentration of 1% (w/v). The resulting mixture was further incubated on ice for 30 min. Cell debris and precipitates were removed from the lysate by centrifugation at 45,000 × *g* at 4 °C for 30 min. Ammonium sulfate was added to the supernatant to a final saturation of 55%, and the solution was incubated on ice for 60 min. The precipitated protein was collected by centrifugation at 45,000 × *g* at 4 °C for 30 min. The obtained precipitate was dissolved in 4 mL of 20 mM Tris-HCl buffer (pH = 7.4, adjusted at 4 °C) and dialyzed against 2 L of 20 mM Tris-HCl buffer (pH = 7.4) three times at 4 °C for 4 h, 4 h, and 12 h. The resulting solution was diluted with 26 mL of 20 mM Tris-HCl buffer (pH = 7.4). After centrifugation at 45,000 × *g* at 4 °C for 10 min, the supernatant was passed through a 0.22 μm filter. The filtered solution was loaded onto a column packed with 30 mL of Bio-Rad Macro-Prep High Q anion exchange resin, which had been pre-equilibrated in 20 mM Tris-HCl buffer (pH = 7.4). The flow-through fraction was collected and buffer-exchanged into 10 mM MOPS buffer (pH = 7.9) by dialysis (8 kDa cutoff). The obtained sample was concentrated using an Amicon Ultra-15 (10 kDa cutoff) centrifugal filter unit to reach a final concentration of 300 μM MIF trimer. The purified protein solution was stored at −80 °C. The concentrations of the purified proteins were determined using the calculated absorption coefficients at 280 nm based on their amino acid sequences (38,850 $M^{-1}cm^{-1}$ for WT MIF trimer and 34,380 $M^{-1}cm^{-1}$ for the S61H/Y100H and Y100H variants). MIF variants were crystallized at 20 °C using hanging-drop vapor-diffusion method. Crystals were obtained using a reservoir solution containing 2.0 M ammonium sulfate, 20 mM Tris-HCl buffer (pH = 7.5), and 3% isopropanol. The hanging-drop solution contained 1.9 μL of the protein solution (1.0 mM) in 20 mM Tris-HCl buffer (pH = 7.0) and 1.9 μL of the reservoir solution. For Zn_3-MIF(S61H/Y100H)-L (PDB code: 9JIY) and Zn_3-MIF(Y100H) (PDB code: 9JJ0), 0.2 μL of 100 mM $ZnCl_2$ (10.5 eq. per MIF monomer) was added to the hanging drop solution. For Zn_3-MIF(S61H/Y100H) (PDB code: 9JIZ), 0.5 μL of 100 mM $ZnCl_2$ (26.0 eq. per MIF monomer) was added to the hanging-drop solution.

DLS measurements

Protein solutions were placed in plastic DTS0012 cuvettes or ZMV1002 quartz cells (both from Malvern Panalytical Ltd.) and maintained at 20 °C for at least 3 min before light scattering was measured.

ITC measurements

MIF trimer (50 μM in 5 mM MOPS buffer (pH = 7.9)) was titrated with $ZnCl_2$ (1.7 mM in 5 mM MOPS buffer (pH = 7.9)) using a Malvern Panalytical MicroCal PEAQ-ITC. The cell was filled with MIF, and a syringe was filled with a zinc solution. The zinc solution was injected 13 times in portions of 3 μL (6 s duration and 210 s spacing). The obtained data were analyzed using the Malvern Panalytical MicroCal PEAQ-ITC analysis software.

Reaction conditions for the hydrolysis experiments

Experiments were performed in reaction mixtures where the final concentrations of each component were: MIF trimer (50 μM); $ZnCl_2$ (0-400 μM); *p*-nitrophenyl acetate (pNA) (0.2–8 mM); and NaCl or KCl (0-96 mM). In more detail, a Zn_x-MIF stock solution and pNA stock solution were freshly prepared using the conditions listed in

Supplementary Tables 5 and 6, respectively. Using a 12-channel pipet equipped with a mixer (Supplementary Fig. 7), 220 µL of Zn_x-MIF stock solution and 220 µL of pNA stock solution were mixed and then loaded directly into an Eppendorf UVette® cuvette set in an Agilent Technologies Cary 3500 spectrophotometer equipped with a thermostatic cell holder maintained at 25 °C. The absorption changes at 405 nm as a function of time were recorded for 90 s at 0.1 s intervals. The concentrations of *p*-nitrophenol at each pH were determined based on the calibration curves (Supplementary Fig. 8).

Reaction conditions for the tautomerization reactions

Experiments were performed under reaction conditions where the final concentrations in the reaction mixture are: MIF trimer (50 nM); $ZnCl_2$ (50 µM); and *p*-hydroxyphenylpyruvic acid (2 mM). In more detail, the Zn_x-MIF stock solution was prepared using the conditions listed in Supplementary Table 7. The mixtures listed in Supplementary Table 8 were prepared in an Eppendorf UVette® cuvette set in an Agilent Technologies Cary 3500 spectrophotometer equipped with a thermostatic cell holder maintained at 20 °C. The absorption changes at 306 nm as a function of time were recorded for 60 s at 0.1 s intervals. The concentrations of the product were determined based on the previously reported absorption coefficient at 306 nm (11400 $M^{-1}cm^{-1}$)[50].

Reporting summary

Further information on research design is available in the Nature Portfolio Reporting Summary linked to this article.

Data availability

The crystallography data generated in this study have been deposited in the Protein Data Bank under accession codes 9JIT, 9JIV, 9JIY, 9JIZ, and 9JJ0. All other data reported in this study are available in the main text, the Supplementary Information, or Source Data. Source data are provided with this paper.

Code availability

The Python code of the geometric screening is available as Supplementary Code.

References

1. McWilliams, S. F. & Holland, P. L. Dinitrogen binding and cleavage by multinuclear iron complexes. *Acc. Chem. Res.* **48**, 2059–2065 (2015).
2. Ohki, Y. et al. Nitrogen reduction by the Fe sites of synthetic $[Mo_3S_4Fe]$ cubes. *Nature* **607**, 86–90 (2022).
3. Cook, S. A. & Borovik, A. S. Molecular designs for controlling the local environments around metal ions. *Acc. Chem. Res.* **48**, 2407–2414 (2015).
4. Fujisaki, H. et al. Selective methane oxidation by molecular iron catalysts in aqueous medium. *Nature* **616**, 476–481 (2023).
5. Schwizer, F. et al. Artificial metalloenzymes: reaction scope and optimization strategies. *Chem. Rev.* **118**, 142–231 (2018).
6. Chen, D. et al. An evolved artificial radical cyclase enables the construction of bicyclic terpenoid scaffolds via an H-atom transfer pathway. *Nat. Chem*. https://doi.org/10.1038/s41557-024-01562-5. (2024).
7. Ji, P., Park, J., Gu, Y., Clark, D. S. & Hartwig, J. F. Abiotic reduction of ketones with silanes catalysed by carbonic anhydrase through an enzymatic zinc hydride. *Nat. Chem.* **13**, 312–318 (2021).
8. Longwitz, L., Leveson-Gower, R. B., Rozeboom, H. J., Thunnissen, A.-M. W. H. & Roelfes, G. Boron catalysis in a designer enzyme. *Nature* **629**, 824–829 (2024).
9. Trimble, J. S. et al. A designed photoenzyme for enantioselective [2+2] cycloadditions. *Nature* **611**, 709–714 (2022).
10. Sun, N. et al. Enantioselective [2+2]-cycloadditions with triplet photoenzymes. *Nature* **611**, 715–720 (2022).
11. Oohora, K. & Hayashi, T. Myoglobins engineered with artificial cofactors serve as artificial metalloenzymes and models of natural enzymes. *Dalton Trans.* **50**, 1940–1949 (2021).
12. Srivastava, P., Yang, H., Ellis-Guardiola, K. & Lewis, J. C. Engineering a dirhodium artificial metalloenzyme for selective olefin cyclopropanation. *Nat. Commun.* **6**, 7789 (2015).
13. Yamamura, K. & Kaiser, E. T. Studies on the oxidase activity of copper(II) carboxypeptidase A. *J. Chem. Soc., Chem. Commun*. 830 https://doi.org/10.1039/c39760000830. (1976).
14. Okrasa, K. & Kazlauskas, R. J. Manganese-substituted carbonic anhydrase as a new peroxidase. *Chem. Eur. J.* **12**, 1587–1596 (2006).
15. Fernández-Gacio, A., Codina, A., Fastrez, J., Riant, O. & Soumillion, P. Transforming carbonic anhydrase into epoxide synthase by metal exchange. *ChemBioChem* **7**, 1013–1016 (2006).
16. Fujieda, N. et al. A Well-defined osmium–cupin complex: hyperstable artificial osmium peroxygenase. *J. Am. Chem. Soc.* **139**, 5149–5155 (2017).
17. Song, W. J. & Tezcan, F. A. A designed supramolecular protein assembly with in vivo enzymatic activity. *Science* **346**, 1525–1528 (2014).
18. Zastrow, M. L., Peacock, A. F. A., Stuckey, J. A. & Pecoraro, V. L. Hydrolytic catalysis and structural stabilization in a designed metalloprotein. *Nat. Chem.* **4**, 118–123 (2012).
19. Rufo, C. M. et al. Short peptides self-assemble to produce catalytic amyloids. *Nat. Chem.* **6**, 303–309 (2014).
20. Studer, S. et al. Evolution of a highly active and enantiospecific metalloenzyme from short peptides. *Science* **362**, 1285–1288 (2018).
21. Jeong, W. J. & Song, W. J. Design and directed evolution of non-canonical β-stereoselective metalloglycosidases. *Nat. Commun.* **13**, 6844 (2022).
22. Caldwell, S. J. et al. Tight and specific lanthanide binding in a de novo TIM barrel with a large internal cavity designed by symmetric domain fusion. *Proc. Natl. Acad. Sci. USA* **117**, 30362–30369 (2020).
23. Yeung, N. et al. Rational design of a structural and functional nitric oxide reductase. *Nature* **462**, 1079–1082 (2009).
24. Mirts, E. N., Petrik, I. D., Hosseinzadeh, P., Nilges, M. J. & Lu, Y. A designed heme-[4Fe-4S] metalloenzyme catalyzes sulfite reduction like the native enzyme. *Science* **361**, 1098–1101 (2018).
25. Lombardi, A., Pirro, F., Maglio, O., Chino, M. & DeGrado, W. F. De novo design of four-helix bundle metalloproteins: one scaffold, diverse reactivities. *Acc. Chem. Res.* **52**, 1148–1159 (2019).
26. Reig, A. J. et al. Alteration of the oxygen-dependent reactivity of de novo Due Ferri proteins. *Nat. Chem.* **4**, 900–906 (2012).
27. Ulas, G., Lemmin, T., Wu, Y., Gassner, G. T. & DeGrado, W. F. Designed metalloprotein stabilizes a semiquinone radical. *Nat. Chem.* **8**, 354–359 (2016).
28. Zhang, S.-Q. et al. De novo design of tetranuclear transition metal clusters stabilized by hydrogen-bonded networks in helical bundles. *J. Am. Chem. Soc.* **140**, 1294–1304 (2018).
29. Pirro, F. et al. A de novo-designed type 3 copper protein tunes catechol substrate recognition and reactivity. *Angew. Chem. Int. Ed.* **62**, e202211552 (2023).
30. Abe, S. et al. Polymerization of phenylacetylene by rhodium complexes within a discrete space of apo-ferritin. *J. Am. Chem. Soc.* **131**, 6958–6960 (2009).
31. Choi, T. S. & Tezcan, F. A. Overcoming universal restrictions on metal selectivity by protein design. *Nature* **603**, 522–527 (2022).
32. Hoffnagle, A. M. & Tezcan, F. A. Atomically accurate design of metalloproteins with predefined coordination geometries. *J. Am. Chem. Soc.* **145**, 14208–14214 (2023).

33. Jeffery, C. J. Moonlighting proteins. *Trends Biochem. Sci.* **24**, 8–11 (1999).
34. Krishna, R. et al. Generalized biomolecular modeling and design with RoseTTAFold All-Atom. *Science* **384**, eadl2528 (2024).
35. Okamoto, Y. et al. A cell-penetrating artificial metalloenzyme regulates a gene switch in a designer mammalian cell. *Nat. Commun.* **9**, 1943 (2018).
36. Chang, T., Vong, K., Yamamoto, T. & Tanaka, K. Prodrug activation by gold artificial metalloenzyme-catalyzed synthesis of phenanthridinium derivatives via hydroamination. *Angew. Chem., Int. Ed.* **60**, 12446–12454 (2021).
37. Coleman, J. E. Zinc proteins: enzymes, storage proteins, transcription factors, and replication proteins. *Annu. Rev. Biochem.* **61**, 897–946 (1992).
38. Zastrow, M. L. & Pecoraro, V. L. Designing hydrolytic zinc metalloenzymes. *Biochemistry* **53**, 957–978 (2014).
39. Zastrow, M. L. & Pecoraro, V. L. Influence of active site location on catalytic activity in de novo-designed zinc metalloenzymes. *J. Am. Chem. Soc.* **135**, 5895–5903 (2013).
40. Basler, S. et al. Efficient Lewis acid catalysis of an abiological reaction in a de novo protein scaffold. *Nat. Chem.* **13**, 231–235 (2021).
41. Der, B. S., Edwards, D. R. & Kuhlman, B. Catalysis by a de novo zinc-mediated protein interface: implications for natural enzyme evolution and rational enzyme engineering. *Biochemistry* **51**, 3933–3940 (2012).
42. Weston, J. Mode of action of bi- and trinuclear zinc hydrolases and their synthetic analogues. *Chem. Rev.* **105**, 2151–2174 (2005).
43. Liu, X., Du, P. & Cao, R. Trinuclear zinc complexes for biologically relevant μ^3-oxoanion binding and carbon dioxide fixation. *Nat. Commun.* **4**, 2375 (2013).
44. Calandra, T. & Roger, T. Macrophage migration inhibitory factor: a regulator of innate immunity. *Nat. Rev. Immunol.* **3**, 791–800 (2003).
45. Lubetsky, J. B., Swope, M., Dealwis, C., Blake, P. & Lolis, E. Pro-1 of macrophage migration inhibitory factor functions as a catalytic base in the phenylpyruvate tautomerase activity. *Biochemistry* **38**, 7346–7354 (1999).
46. Park, H. et al. PAAN/MIF nuclease inhibition prevents neurodegeneration in Parkinson's disease. *Cell* **185**, 1943–1959.e21 (2022).
47. Meza-Romero, R. et al. Modeling of both shared and distinct interactions between MIF and its homologue D-DT with their common receptor CD74. *Cytokine* **88**, 62–70 (2016).
48. Pantouris, G. et al. Regulation of MIF enzymatic activity by an allosteric site at the central solvent channel. *Cell Chem. Biol.* **27**, 740–750.e5 (2020).
49. Schoonen, L. et al. Alternative application of an affinity purification tag: hexahistidines in ester hydrolysis. *Sci. Rep.* **7**, 14772 (2017).
50. Parkins, A. & Pantouris, G. Protocol for purification and enzymatic characterization of members of the human macrophage migration inhibitory factor superfamily. *STAR Protoc.* **4**, 102375 (2023).
51. Scheller, L. & Fussenegger, M. From synthetic biology to human therapy: engineered mammalian cells. *Curr. Opin. Biotechnol.* **58**, 108–116 (2019).
52. Frisch, M. J. et al. Gaussian 16 Rev. C.01. (2016).
53. Huang, J. et al. Charmm36m: an improved force field for folded and intrinsically disordered proteins. *Nat. Methods* **14**, 71–73 (2017).
54. Plimpton, S. Fast parallel algorithms for short-range molecular dynamics. *J. Comp. Phys.* **117**, 1–19 (1995).
55. Nosé, S. A. Molecular-dynamics method for simulations in the canonical ensemble. *Mol. Phys.* **52**, 255–268 (1984).
56. Hoover, W. G. Constant-pressure equations of motion. *Phys. Rev. A* **34**, 2499–2500 (1986).
57. Martyna, G. J., Tobias, D. J. & Klein, M. L. Constant pressure molecular dynamics algorithms. *J. Chem. Phys.* **101**, 4177–4189 (1994).
58. Parrinello, M. & Rahman, A. Polymorphic transitions in single crystals: a new molecular dynamics method. *J. Appl. Phys.* **52**, 7182–7190 (1981).
59. Hockney, R. W. & Eastwood, J. W. Computer simulation using particles. (Hilger: Bristol, 1989).
60. Verlet, L. Computer "experiments" on classical fluids. I. Thermodynamical properties of Lennard-Jones molecules. *Phys. Rev.* **159**, 98–103 (1967).
61. Ryckaert, J.-P., Ciccotti, G. & Berendsen, H. J. C. Numerical integration of the Cartesian equations of motion of a system with constraints: molecular dynamics of *N*-alkanes. *J. Comp. Phys.* **23**, 327–341 (1977).
62. Smart, O. S., Neduvelil, J. G., Wang, X., Wallace, B. A. & Sansom, M. S. P. Hole: a program for the analysis of the pore dimensions of ion channel structural models. *J. Mol. Graph.* **14**, 354–360 (1996).
63. Humphrey, W., Dalke, A. & Schulten, K. Vmd: visual molecular dynamics. *J. Mol. Graph.* **14**, 33–38 (1996).

Acknowledgements

Y.O., T.M., and T.I. acknowledge generous support from the Frontier Research Institute for Interdisciplinary Sciences (FRIS), Tohoku University. Y.O. and T.M. gratefully acknowledge support from the Tohoku Initiative for Fostering Global Researchers for Interdisciplinary Sciences (TI-FRIS) of MEXT's Strategic Professional Development Program for Young Researchers. Y.O. gratefully acknowledges JST ACT-X (JPMJAX1913), JST PRESTO (JPMJPR22A4), and JSPS Grants-in-Aid for Scientific Research (21H05118). T.M. gratefully acknowledges the JST FOREST Program (JPMJFR212H). T.H. gratefully acknowledges JSPS Grants-in-Aid for Scientific Research (24K08609). Generous support from the FRIS CoRE, which is a shared research environment, as well as Prof. Shinsuke Niwa's group at Tohoku University is acknowledged. A part of this work was conducted at the Institute for Molecular Science, supported by Advanced Research Infrastructure for Materials and Nanotechnology in Japan (JPMXP1223MS1070) of the Ministry of Education, Culture, Sport, Science and Technology (MEXT), Japan. Prior to submission, this manuscript has been revised by a professional language-editing service (www.mayerscientificediting.com). Synchrotron experiments were conducted at beamlines BL44XU, BL41XU, and BL45XU at SPring-8 (Hyogo, Japan) in collaboration with the Institute for Protein Research at Osaka University and the Japan Synchrotron Radiation Research Institute. This research was supported by Joint Research of the Exploratory Research Center on Life and Living Systems (ExCELLS). (ExCELLS program No, 25EXC604).

Author contributions

Y.O. conceived, designed, and directed the overall project. A.U., F.T., and Y.O. designed and performed the experiments and analyzed the results, except for those specifically noted below. T.M. and Y.O. designed and performed the computational design of the designer multimetalloenzymes. T.H. performed the X-ray crystal-structure analysis and DLS measurements. T.I. designed and prepared a mixing unit for the enzymatic reactions. T.K. designed the mathematical models and analyzed the kinetic parameters. T.M., T.H., T.K., and Y.O. wrote the manuscript; all authors have given approval to the final version of the manuscript.

Competing interests

The authors declare no competing interests.

Additional information

Supplementary information The online version contains supplementary material available at https://doi.org/10.1038/s41467-025-61909-5.

Correspondence and requests for materials should be addressed to Tomoki Himiyama, Takuya Mabuchi or Yasunori Okamoto.

Peer review information *Nature Communications* thanks Erik Donovan Hedegård, who co-reviewed with Gabriel Rodriguesand the other, anonymous, reviewer(s) for their contribution to the peer review of this work. A peer review file is available.